Three-Dimensional Mapping of the Light Intensity Transmitted through Nanoapertures

Dragos Amarie,[†,§] Nathan D. Rawlinson,[‡,§] William L. Schaich,[†] Bogdan Dragnea,*[,‡] and Stephen C. Jacobson*[,‡]

Department of Chemistry and Department of Physics, Indiana University, Bloomington, Indiana 47405

ABSTRACT

A general method to map the 3D spatial distribution of light emerging from nanoscale apertures is presented that uses photolithographic techniques to create polymer replicas of the intensity distribution. The resulting features varied with aperture diameter and exposure time and showed good correlation with theory. This method provides direct visualization of the intensity distribution in close proximity to nanostructures and overcomes limitations imposed by physical probes where the contribution of the probe to the map requires deconvolution.

For the past two decades, the interaction of light with nanostructured materials has been an area of intense theoretical and experimental investigation, and the progress has been summarized in several reviews.[1−3] The behavior of surface-bound electromagnetic fields allows a number of technologically important applications including subdiffraction resolution in optical imaging,[4−7] sensitivity to differences in surface modifications exploited in surface plasmon sensors,[8,9] enormous signal enhancements associated with surface-enhanced Raman scattering (SERS),[10−12] and enhanced transmission of subwavelength aperture arrays in metal films.[13−15] In addition, these phenomena have been applied recently to emerging fields such as zero-mode waveguide bioanalytical spectroscopy[16] and near-field trapping and manipulation.[17−19] The continued development of these areas requires a detailed understanding and experimental control of the spatial field distribution in the vicinity of nanostructures. However, despite significant effort, the ability to map the light intensity in a way that allows a direct comparison with theoretical predictions has remained elusive. The main reason for this is that the majority of experiments have used proximity probes whose physical properties have to be taken into account by theoretical models in order to produce an accurate representation of the intensity distribution. In this report, we introduce a method able to provide a 3D spatial map of the light intensity in close proximity to nanostructures without the need for physical probes. This method works from near-field to far-field regimes and shows encouraging agreement with theoretical calculations over the entire range.

The method is based on the lithographic mapping of local photochemical changes occurring in a chemically amplified polymeric resist exposed to light scattered by a nanostructured surface. Here, we describe an application of this technique to an ensemble of small apertures in a metal film supported by a glass substrate. The method is, however, applicable to surfaces of arbitrary roughness, does not involve a proximity probe perturbing the field, and is limited in resolution primarily by the characteristics of the polymer resist.

By providing a direct means to make physical measurements of the intensity spatial distribution, the method overcomes many of the limitations of near-field scanning optical microscopy (NSOM) for mapping field intensity near surface nanostructures. Although NSOM has been instrumental to the understanding of light interaction with nanostructures, there exist several challenges. First, the optical response of an NSOM apparatus is a function of both the sample and tip geometries as well as of the chemical composition of each. In many cases, numerical computations are required for accurate image interpretation.[1] Second, surfaces with rich morphologies (e.g., those on which SERS is observed) represent difficult samples for NSOM because of the possible cross talk between the optical and topographical signals and related artifacts.[20] Third, several factors including low sensitivity to dielectric constant changes, field penetration into the metal coat or tip, and the size of the probe account for a practical resolution for NSOM of roughly 100 nm, reaching ∼10 nm in limited cases.[2,7,21]

In this report, we have two principal aims: (1) to describe the experimental conditions required for 3D photolithographic mapping and (2) to demonstrate by comparison with a theoretical model that the method yields useful polymeric

* To whom correspondence should be addressed. E-mail: dragnea@indiana.edu, jacobson@indiana.edu.
† Department of Physics.
‡ Department of Chemistry.
§ These authors contributed equally.
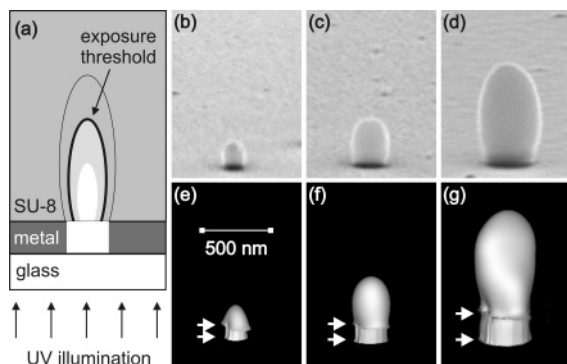
Figure 1. (a) Schematic of the experimental setup for lithographic mapping of the transmitted intensity through nanoapertures. Scanning electron micrographs are shown for pillars resulting from aperture diameters of (b) 110, (c) 200, and (d) 360 nm. The features shown were exposed for 3 min to UV light. (e−g) Three-dimensional isointensity surfaces of the light obtained from finite-difference time-domain calculations for the same conditions used for the pillars in b−d. The arrows indicate the top and bottom of the metal film. The size bar is the same for the experiments and calculations, and the schematic is not to scale.

Figure 2. Variation of measured pillar height with aperture diameter for exposure times of 1, 3, 10, and 30 min. The pillar heights were measured using a scanning electron microscope (SEM), and the error bars are $\pm\sigma$ for at least 20 pillars.

replicas of the transmitted light intensity distribution. The theoretical model employs a single fit parameter (the exposure threshold for significant photoresist cross-linking) and does not depend on the photochemical response of the chemically amplified resist. However, one takes advantage of a well-defined exposure threshold for the resist,[22] allowing direct photolithographic mapping with high spatial resolution.

Using nanosphere lithography,[23,24] randomly dispersed nanoapertures were fabricated in a metal film supported on a glass substrate as follows. Polystyrene nanospheres ranging in diameter from 110 to 770 nm were first dispersed on a glass substrate. Next, a thin chromium adhesion layer and an aluminum overlayer were thermally evaporated on top of the dispersed nanospheres. The thickness of the metal film ranged from 50 $\pm$ 10 nm for the 110 nm nanospheres to 380 $\pm$ 10 nm for the 770 nm nanospheres. Finally, the nanospheres were removed by sonication, leaving behind transparent apertures in the evaporated metal film. The aperture diameters were equal to the nanosphere diameters. Nanosphere lithography provides high-quality apertures with reproducible optical properties,[25] and the Supporting Information further details aperture fabrication.[26] A negative-tone photoresist (SU-8) was then spin coated on top of the metal film, and the photoresist was exposed to UV light through the nanoapertures from the opposite side (Figure 1a). The light source was a high-pressure Hg lamp whose primary wavelength is 365 nm. Light that emerged through the apertures was sufficient to generate a latent photochemical image that, in turn, was amplified and developed during subsequent processing steps of the photoresist (postexposure baking and dissolution). Elsewhere, the metal film effectively blocked light transmission where apertures were absent. Panels b−d of Figure 1 show a set of pillar-shaped resist features obtained for a 3 min exposure time with aperture diameters of 110, 200, and 360 nm. Diameters ranging from subwavelength to superwavelength size were used to probe regimes dominated by near- and far-field characteristics of the transmitted light, respectively. We remark that the photoresist film thickness (∼15 μm) was always greater than
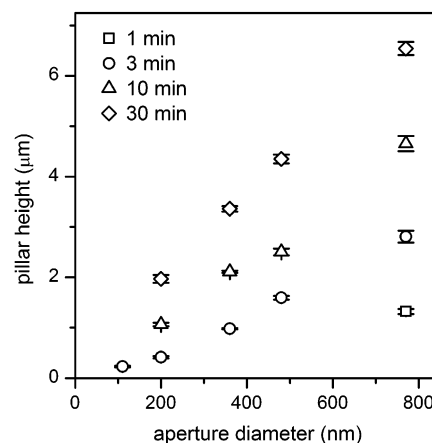
the height of the tallest features (6.54 μm). This is in contrast with the more established contact printing lithography where the film thickness determines the height of the features.[22]

We studied aperture sizes of 110, 200, 360, 480, and 770 nm and exposure times of 1, 3, 10, and 30 min. The polymeric structures obtained ranged in height from 0.23 μm for the 110 nm aperture and 3 min exposure time to 6.54 μm for the 770 nm aperture and 30 min exposure time. Figure 2 shows the variation of pillar height with aperture diameter for different exposure times and includes all cases where stable, well-defined pillars were obtained. As seen in Figure 2, the pillar heights grew with increasing aperture diameter and increasing exposure time. For the shortest exposure time of 1 min, free-standing pillars were not generated for the 110 to 480 nm aperture diameters because of insufficient cross-linking of the polymer to remain intact during post-exposure processing. Also, for exposure times longer than 3 min, discernible pillar formation was not observed for the 110 nm aperture. In this case, the 50 nm metal film was too thin and/or porous, allowing cross-linking of the entire SU-8 film independent of the presence of apertures. This limitation is not intrinsic to the mapping method but can be attributed to the nanosphere lithography, which requires the metal film thickness to be less than the radius of the nanosphere. Other methods such as focused ion beam milling or electron beam lithography could be used to generate apertures in metal films of arbitrary thickness without the same film thickness constraint as in nanosphere lithography and are, therefore, potentially better for creating finer structures (e.g., less than 100 nm).

We now turn our attention to how one can relate pillar shapes to electric fields. Our view relies on the hypothesis that the changes at any point in the photoresist during exposure to light are proportional to the local exposure, Φ, defined as

$$\Phi = t|\vec{E}|^2 \tag{1}$$

where t is the exposure time and $|\vec{E}|^2$ is the electric field intensity above the aperture in steady state. After exposure

and postexposure processing, regions of small Φ (soluble resist) are separated from regions of large Φ (insoluble resist) by a boundary surface determined by an exposure threshold, Φ_{th}. The specific value of Φ_{th} depends on both the resist material and the processing steps. Because the preexposure bake, postexposure bake, and developing conditions were kept constant in the experiments, we can assume that the exposure threshold was the same for all samples. Thus, with different exposure times, the pillar shape should represent different isointensity surfaces of the transmitted light. For a sequence of increasing exposure times and $\Phi = \Phi_{th}$, the values of $|\vec{E}|^2$ on the isosurfaces decrease, and the growth and reshaping of the resultant pillars reveal the distribution of light intensity.

As a first illustration of such an analysis, we apply it to a rough estimate of the intensity directly above the aperture at a distance z from the metal film

$$|\vec{E}(x = y = 0, z > 0)|^2 \approx T(d)|\vec{E}_i|^2 \frac{d^2}{d^2 + z^2} \qquad (2)$$

where $|\vec{E}_i|^2$ is the intensity of the incident beam, d is the aperture diameter, and $T(d)$ is the aperture transmission efficiency defined as the ratio of the flux transmitted into the far field to the flux incident on the aperture. We expect from Bethe−Bouwkamp theory[27] that $T(d)$ rapidly decreases for diameters smaller than the wavelength of the light. At the opposite extreme, where Bethe−Bouwkamp theory does not hold, $T(d)$ should saturate at ~ 1. The intersection of the exposure threshold isosurface ($\Phi = \Phi_{th}$) with the surface normal centered on the aperture gives the pillar height, h. Combining eqs 1 and 2, one obtains for long exposure times that the pillar height is given asymptotically by

$$h \approx d \left[\frac{T(d)|\vec{E}_i|^2 t}{\Phi_{th}} \right]^{1/2} \qquad (3)$$

For a fixed diameter, the pillar height should vary as $t^{1/2}$. Thus, our hypothesis leads to an explicit approximate estimate of how the pillar height depends on the aperture diameter and exposure time.

Before comparing with the experimental data, we describe how a better theoretical estimate can be made (i.e., how eq 2 can be improved). For this we have used finite-difference time-domain (FDTD) calculations[28] to obtain isointensity surfaces corresponding to our experimental conditions. These calculations were performed for a fixed incident field strength and linear polarization with variable aperture diameter and metal film thickness.[26] For the 3 min exposure time at which we have data for all aperture diameters, we used the experimental pillar heights seen in Figure 3 to evaluate $|\vec{E}(x = y = 0, h)|^2$ and to estimate the exposure threshold, Φ_{th}, from eq 1. Applying a least-squares fitting procedure to a set of Φ_{th} estimates for the measured pillar heights, we found a best fit value of Φ_{th}. This single value for the exposure threshold was then used to produce isointensity surfaces for different exposure times and aperture diameters. Panels e−g of Figure 1 show the calculated isointensity surfaces corresponding to the experimentally generated pillars in panels
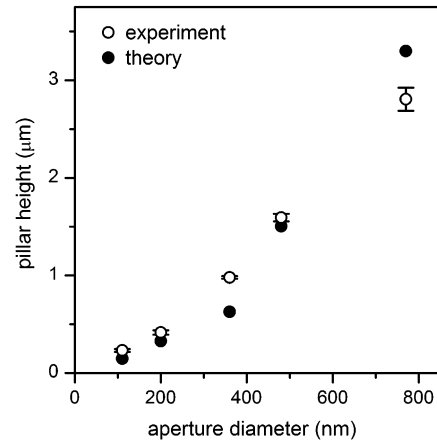
Figure 3. Comparison between experiment and theory of the variation of pillar height with aperture diameter for an exposure time of 3 min. The experimental data are from Figure 2, and the theory points are from finite-difference time-domain (FDTD) calculations using a single value for the exposure threshold, Φ_{th}, obtained from the experimental data with a nonlinear least-squares fit.
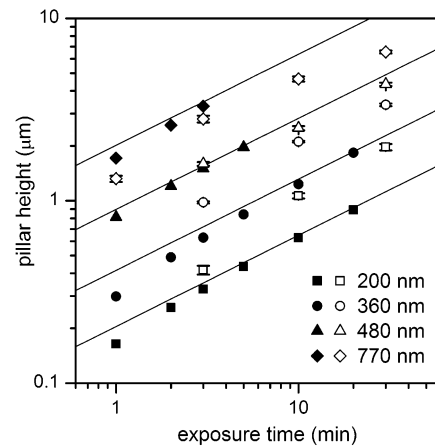
Figure 4. Comparison between experiment (open symbols) and theory (solid symbols) of the variation of the pillar height with exposure time for aperture diameters of 200, 360, 480, and 770 nm. The theoretical points are determined from FDTD calculations using a single value of Φ_{th}. The straight lines describe the asymptotic behavior of the simulations where $h \propto t^{1/2}$. The pillar heights were measured using an SEM, and the error bars are $\pm \sigma$ for at least 20 pillars.

b−d of Figure 1, respectively. A comparison of the experimental and predicted pillar heights for the 3 min exposure time is shown in Figure 3, and there is good agreement between theory and experiment.

In Figure 4, the measured and theoretical pillar heights are compared for the entire range of experimental parameters examined and are plotted as a function of exposure time for the different aperture diameters. Results from explicit FDTD calculations are shown as points and extend to only modest values of the pillar height. We are presently limited to calculating pillars with a height of approximately 3 μm. However, Green's theorem can be used to extract the limiting behavior of $|\vec{E}|^2$ far into the resist.[28] Specifically, $|\vec{E}(x = y = 0, z \gg d)|^2 \rightarrow C(d)/z^2$ where the constant C is determined from an integral over x and y of the fields at fixed, small $z > 0$. The lines in Figure 4 are then set by $h = [tC(d)/\Phi_{th}]^{1/2}$,

and the individual simulation points clearly merge into these asymptotic lines as the exposure time increases. At the other extreme for short exposure times, the pillar heights grow more rapidly with exposure time because one is probing the distribution of $|\bar{E}|^2$ near its maximum value. This qualitative behavior is also implied by the simpler eq 2 for $z < d$.

For the experimental points at intermediate aperture diameters (360 and 480 nm) in Figure 4, one sees that $h(t)$ is reasonably represented by a $t^{1/2}$ dependence. However, the growth of the pillar height with exposure time is somewhat slower than $t^{1/2}$ for the largest aperture (770 nm) and somewhat faster than $t^{1/2}$ for the smallest aperture (200 nm). The other qualitative trend seen in Figures 3 and 4 is that at a fixed exposure time the experimental data lie below theory for larger apertures and above theory for smaller apertures. We are currently studying possible reasons for these differences. First, the structural integrity of the pillars depends on the gradients of light intensity. Smaller pillars have steeper gradients and possibly better structural integrity than larger pillars. Second, the optical response of the thin metal films may not be adequately described by the bulk optical properties used in the calculations. For instance, imperfections in the films could modify the coupling to surface modes. Third, the light used in the experiment is not monochromatic, and the transmission through the aperture is wavelength-dependent. To improve the agreement, future calculations should incorporate a multiwavelength spectrum, or the experiments should be repeated with a monochromatic source (e.g., a laser).

Presently, the spatial resolution of the intensity mapping method is limited by either the response of the polymeric resist or the postdevelopment characterization method. In our case, the limit was set by the spatial resolution, ∼20 nm, of the scanning electron microscope employed to measure the polymeric replicas. However, we believe that with other microscopy methods using material contrast and having better spatial resolution, such as scanning tunneling microscopy and atomic force microscopy, the spatial resolution could be significantly improved down to the 1−10 nm scale. This would, for example, allow the characterization of the "hot spots" postulated for SERS effective surfaces.

In conclusion, photolithographic intensity mapping provides direct access to the spatial distribution of the light in close proximity to nanostructures. We described conditions in which polymer replicas of isointensity surfaces of light transmitted through nanoapertures can be obtained. Encouraging agreement has been found in direct comparisons between the numerical simulations of isointensity surfaces and photolithographic polymeric features indicating that the method may not need a subsequent modeling step to extract the true intensity spatial distribution. The method can also be used on engineered surfaces as a simple tunable way to generate submicrometer-scale features in materials that can be designed a priori with the help of electromagnetic computations able to deal with near-field interference. We believe that several fields including nanoimprinting, photo-nics, sensing, and microfluidics may benefit from this mapping technique and the ability to create features with tunable dimensions.

Supporting Information Available: More detailed descriptions of the feature fabrication and theoretical calculations. This material is available free of charge via the Internet at http://pubs.acs.org.

References

(1) Girard, C.; Dereux, A. *Rep. Prog. Phys.* **1996**, *59*, 657−699.
(2) Dunn, R. C. *Chem. Rev.* **1999**, *99*, 2891−2928.
(3) Girard, C.; Joachim, C.; Gauthier, S. *Rep. Prog. Phys.* **2000**, *63*, 893−938.
(4) Pohl, D. W.; Denk, W.; Lanz, M. *Appl. Phys. Lett.* **1984**, *44*, 651−653.
(5) Betzig, E.; Trautman, J. K.; Harris, T. D.; Weiner, J. S.; Kostelak, R. L. *Science* **1991**, *251*, 1468−1470.
(6) Novotny, L.; Pohl, D. W.; Hecht, B. *Opt. Lett.* **1995**, *20*, 970−972.
(7) Keilmann, F.; Hillenbrand, R. *Philos. Trans. R. Soc. London, Ser. A* **2004**, *362*, 787−805.
(8) Bohn, P. W. *Annu. Rev. Mater. Sci.* **1997**, *27*, 469−498.
(9) West, J. L.; Halas, N. J. *Annu. Rev. Biomed. Eng.* **2003**, *5*, 285−292.
(10) Emory, S. R.; Nie, S. M. *Anal. Chem.* **1997**, *69*, 2631−2635.
(11) Moskovits, M. *Rev. Mod. Phys.* **1985**, *57*, 783−825.
(12) Doering, W. E.; Nie, S. M. *J. Phys. Chem. B* **2002**, *106*, 311−317.
(13) Ebbesen, T. W.; Lezec, H. J.; Ghaemi, H. F.; Thio, T.; Wolff, P. A. *Nature* **1998**, *391*, 667−669.
(14) Lezec, H. J.; Degiron, A.; Devaux, E.; Linke, R. A.; Martin-Moreno, L.; Garcia-Vidal, F. J.; Ebbesen, T. W. *Science* **2002**, *297*, 820−822.
(15) Ghaemi, H. F.; Thio, T.; Grupp, D. E.; Ebbesen, T. W.; Lezec, H. J. *Phys. Rev. B* **1998**, *58*, 6779−6782.
(16) Levene, M. J.; Korlach, J.; Turner, S. W.; Foquet, M.; Craighead, H. G.; Webb, W. W. *Science* **2003**, *299*, 682−686.
(17) Gu, M.; Haumonte, J. B.; Micheau, Y.; Chon, J. W. M.; Gan, X. S. *Appl. Phys. Lett.* **2004**, *84*, 4236−4238.
(18) Chaumet, P. C.; Rahmani, A.; Nieto-Vesperinas, M. *Phys. Rev. B* **2002**, *66*, 195405.
(19) Kwak, E.-S.; Onuta, T.-D.; Amarie, D.; Potyrailo, R.; Stein, B.; Jacobson, S. C.; Schaich, W. L.; Dragnea, B. *J. Phys. Chem. B* **2004**, *108*, 13607−13612.
(20) Hecht, B.; Bielefeldt, H.; Inouye, Y.; Pohl, D. W.; Novotny, L. *J. Appl. Phys.* **1997**, *81*, 2492−2498.
(21) Hillenbrand, R.; Knoll, B.; Keilmann, F. *J. Microsc. (Oxford, U.K.)* **2001**, *202*, 77−83.
(22) Wallraff, G. M.; Hinsberg, W. D. *Chem. Rev.* **1999**, *99*, 1801−1821.
(23) Malinsky, M. D.; Kelly, K. L.; Schatz, G. C.; Van Duyne, R. P. *J. Phys. Chem. B* **2001**, *105*, 2343−2350.
(24) Haynes, C. L.; Van Duyne, R. P. *J. Phys. Chem. B* **2001**, *105*, 5599−5611.
(25) Onuta, T.-D.; Amarie, D.; Dragnea, B. Unpublished data.
(26) Please see Supporting Information.
(27) Bouwkamp, C. J. *Philips Res. Rep.* **1950**, *5*, 321.
(28) Taflove, A.; Hagness, S. C. *Computational Electrodynamics: The Finite-Difference Time-Domain Method*; Artech House: Boston, 2000.

NL050891E